

Three-dimensional MHD flow and heat transfer in a channel with internal obstacle

Alessandro Tassone*, Luciano Gramiccia, Gianfranco Caruso

Department of Astronautical, Electrical and Energy Engineering (DIAEE), Sapienza University of Rome, Corso Vittorio Emanuele II, 244, Rome 00186, Italy

Corresponding Author Email: alessandro.tassone@uniroma1.it

<https://doi.org/10.18280/ijht.360428>

Received: 20 May 2018

Accepted: 24 November 2018

Keywords:

magnetohydrodynamics (MHD), channel flow with obstacle, nuclear fusion reactor, 3D pressure drop, blanket engineering

ABSTRACT

The magnetohydrodynamic flow and heat transfer of a liquid metal in a channel past a circular cylinder with walls of non-uniform conductivity were investigated. The applied magnetic field was transversal to the forced flow (x -direction) and coplanar with the obstacle, featuring non-null components in both the z - and y -directions. Moreover, the cylinder was displaced by the duct centreline toward the bottom wall and its surface was at uniform temperature, so that a ΔT was present between the obstacle and the fluid at the inlet. Non-uniform thickness for the duct-bounding walls is considered which leads to the promotion of jets close to the less-conductive surfaces. The flow features and heat transfer for this case were numerically investigated for different values of the Reynolds number ($20 \leq Re \leq 80$) and Hartmann number ($0 \leq Ha \leq 100$). Their effects on the flow features, pressure drop and heat transfer are analysed and discussed in detail in the present paper. The additional pressure drop introduced by the cylinder presence is found to be independent by Re and decreasing with Ha . Enhanced heat transfer is observed for an increasing Ha with $Nu_{MHD}/Nu = 1.25$. at $Ha = 100$ due to the augmented mass flow rate in the bottom sub-channel.

1. INTRODUCTION

Liquid metals (LM) magnetohydrodynamic (MHD) flows have been extensively studied in the past for their many practical applications, even outside the nuclear industry, which include material processing, electromagnetic pumps and flow meters. The interaction between the moving electro-conductive fluid and an externally applied magnetic field causes the induction of currents in the former and of a volumetric Lorentz force that opposes the fluid motion and triggers the appearance of peculiar flow features on the cross section. These phenomena influence the overall pressure drop and interfere with the heat and mass transport mechanisms [1]. Augmented corrosion and tritium permeation rates, turbulence dampening and heat transfer suppression, severe pressure losses are among the expected outcomes for the transition from the hydrodynamic to the MHD flow regime [2–7]. These effects must be considered to design a LM blanket able to meet the requirements for the implementation a future fusion power plant.

The breeding blanket (BB) is a critical system for a nuclear fusion reactor. Among its main functions, it provides the fusion power removal and conveys it to the primary heat transfer system (PHTS), refrigerates the plasma-facing first wall, ensures the fuel self-sufficiency and cycle closure via tritium breeding, and shields sensible components and personnel from ionizing radiation. Liquid metals are considered as promising working fluids due to their excellent thermal properties and the potential to integrate the role of

coolant, tritium breeder/carrier and neutron multiplier [8]. However, these fluids are considerably more difficult to handle compared with water and/or air and, in particular, the thorough characterization of their behavior in a fusion environment must consider the MHD effects introduced by the molten metal-magnetic field interaction. The pressure drop due to the electromagnetic drag has been recognized early in the development of LM blankets as one of the main parameters driving the design, being orders of magnitude higher than the one due to viscous forces.

In the last years, the efforts of the fusion community have been focused on the “separated” blanket architecture, where the coolant function is fulfilled by a dielectric fluid and the LM is employed exclusively as tritium breeder and carrier. This solution allows to minimize the velocity and electromagnetic drag but, in turn, introduces the necessity to provide an adequate surface for the heat transfer with the coolant. For water-cooled blanket, where the coolant is pressurized at 15.5 MPa, the most widespread strategy foresees pipes immersed in the LM [9-10].

In this framework, the accurate characterization of the flow dynamics and heat transfer for the bounded MHD flow around pipes is of paramount importance to support the blanket design. The most important geometrical parameters that influence the flow features are the blockage ratio (β), the normalized offset of the obstacle from the duct centreline (G/d), and wall thickness (δ_w). This last parameter affects the distribution of the induced currents in the cross-section and, in turn, characterizes the flow pattern around the obstacle.

A typical blanket channel features a magnetic field that is transverse to the main flow direction. The particular case of a unidirectional field aligned with the obstacle axis (spanwise) has been investigated in the past both experimentally and numerically due to its importance for industrial applications, whereas the analogous scenario for a non-unidirectional field, that has both spanwise and transverse components, is almost totally neglected in the literature.

2. PROBLEM FORMULATION

A rectangular duct, defined by a toroidal (z) half-length L and poloidal (y) half-length H , accommodates the obstacle (see Figure 1). The cylinder is hollow, defined by an outer diameter d and inner diameter d_i and aligned with the toroidal axis. The duct walls have non-uniform thickness (δ_w). The cylinder is defined by blockage ratio $\beta = d/2H$ and offset from the duct centerline G/d , where G is the distance between the cylinder bottom and the closest duct wall. The flow is in the radial (x) direction. The upstream (F_u) and downstream (F_d) lengths identify the obstacle radial position in the duct. The problem geometry is shown in Figure 1, whereas Table 1 provides an overview of the geometrical parameters.

Table 1. Geometry parameters and wall conductance ratio

Duct par.	Cylinder par.	Wall δ	$c_w \times 10^2$
[mm]	[mm]	[mm]	
L	d	δ_T	c_T
H	d_i	δ_B	c_B
F_u	G/d	δ_S	c_S
F_d	β	δ_O	c_O

Considering an incompressible fluid with constant thermophysical properties, the dimensionless governing equations for a laminar, inductionless and steady MHD flow can be derived as follows

$$\nabla \cdot \mathbf{u} = 0 \quad (1)$$

$$(\mathbf{u} \cdot \nabla) \mathbf{u} = -\nabla p + \text{Re}^{-1} \nabla^2 \mathbf{u} + \text{Ha}^2 \text{Re}^{-1} (\mathbf{J} \times \mathbf{B}) \quad (2)$$

$$\text{Pe}^{-1} \nabla^2 T - (\mathbf{u} \cdot \nabla) T = 0 \quad (3)$$

$$\nabla^2 \phi - \nabla \cdot (\mathbf{u} \times \mathbf{B}) = 0 \quad (4)$$

$$\mathbf{J} = -\nabla \phi + \mathbf{u} \times \mathbf{B} \quad (5)$$

Here, \mathbf{u} , \mathbf{B} , \mathbf{J} , ϕ , T and p represents the velocity, magnetic induction, current density, electric potential, temperature and pressure scaled by the average inlet velocity u_0 , the modulus of the magnetic induction vector B_0 , $\mathbf{j}_0 = \sigma_0 \mathbf{B}_0$, $\phi_0 = du_0 B_0$, the difference between the local temperature and T_{in} divided by ΔT , and $p_0 = \rho u_0^2$. Lengths are scaled by the external cylinder diameter d , unless otherwise specified, which is also chosen as the length scale for dimensionless parameters. An additional source term in the energy equation (3) would be formally required to represent the Joule heating, but it can be demonstrated that for LM flows it can be neglected [13]. The Reynolds (Re), Hartmann (Ha) and Péclet (Pe) numbers appear in the governing equations and are defined as $\text{Re} = u_0 d / \nu$, $\text{Ha} = B_0 d / (\sigma / \rho \nu)^{0.5}$ and $\text{Pe} = u_0 d / \alpha_t$ where α_t , ν , ρ are the fluid thermal diffusivity, kinematic viscosity and density. An additional quantity, the wall conductance ratio (c_w), is necessary to represent the influence of the electrical boundary conditions on the flow. It can be expressed as $c_w = \sigma_w \delta_w / \sigma L$, with the quantities σ_w and δ_w being the wall electrical conductivity and thickness. The duct considered is bounded by walls of non-uniform thickness, therefore a conductance ratio for each wall must be defined. An unsymmetrical conductance ratio causes the bending of the current paths and, thus, redistribute the flow rate on the duct cross-section toward the least conductive walls [15, 19] (see Table 1).

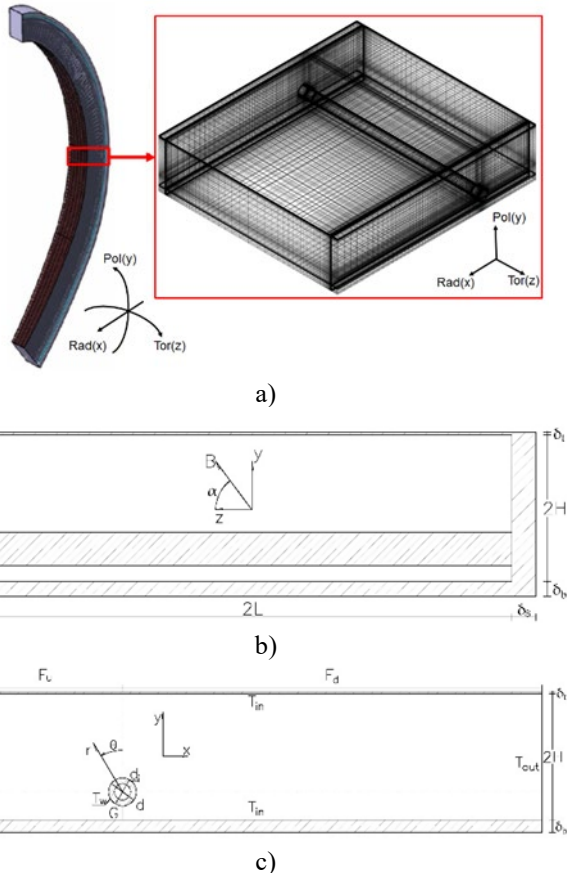


Figure 1. a) Fusion reactor blanket outboard module [10] and test case mesh (left), b) toroidal poloidal (z - y) cross-section and c) radial poloidal (x - y) cross-section

For the former case, a delayed transition to unsteady and turbulent regimes, cylinder wake suppression, and a more stable flow is observed compared with the ordinary hydrodynamic case [11-14]. However, previous studies have been focused mostly on the flow pattern characterization, whereas its effect on the heat transfer has been overlooked.

Recently, Tassone et al. [15-16] have investigated the problem of a forced convection flow about a fixed temperature cylinder of arbitrary conductivity with a transversal skewed magnetic field applied and bounding duct walls of non-uniform thickness for $20 \leq \text{Re} \leq 40$, $0 \leq \text{Ha} \leq 50$ and magnetic field inclination $0^\circ \leq \alpha \leq 32^\circ$. The purpose of this work is to extend and integrate the results presented in the previous papers considering the case of the insulating obstacle up to $\text{Re} = 80$ and $\text{Ha} = 100$ for $\alpha = 16^\circ$. The commercial CFD code ANSYS CFX 15 was employed to perform this study. In recent years, this code has been employed to perform many numerical studies of incompressible MHD flows, while being validated against analytical solutions and experimental data for both pressure-driven and natural convection benchmarks [17-19].

A local Nusselt number is defined to assess the heat transfer between the obstacle and surrounding fluid employing the following relation.

$$Nu_w(\theta, z) = \frac{d}{T_b - T_w} \left. \frac{\partial T}{\partial r} \right|_A \quad (6)$$

Table 2. PbLi and Eurofer properties at $T_{ref} = 558$ K

	PbLi [20]	Eurofer [21]
ρ [kg m ⁻³]	$9.856 \cdot 10^3$	$7.695 \cdot 10^3$
σ [S m ⁻¹]	$7.932 \cdot 10^5$	$1.259 \cdot 10^6$
κ [W m ⁻¹ K ⁻¹]	12.831	30.060
ν [m ² s ⁻¹]	$2.332 \cdot 10^{-7}$	n.a.
α_t [m ² s ⁻¹]	$6.885 \cdot 10^{-6}$	$7.193 \cdot 10^{-6}$
μ [H m ⁻¹]	$4\pi \cdot 10^{-7}$	$4\pi \cdot 10^{-7}$

where the temperature gradient is evaluated in the direction normal to the obstacle external surface (A) and T_{bulk} is the fluid bulk temperature. It is computed as the average temperature on the cylindrical surface S, at distance $r = d$ from the obstacle center, weighted on the velocity distribution

$$T_{bulk} = \frac{\iint_S uT \, d\theta dz}{\iint_S u \, d\theta dz} \quad (7)$$

Accordingly, the average Nusselt number on the whole cylinder external surface is obtained by the integration of (6)

$$Nu = \frac{1}{A} \iint_A Nu_w \, d\theta dz \quad (8)$$

The increase in the pressure drop compared with the empty duct can be defined as the normalized difference between the calculated drop and the one for the unperturbed channel (Δp_{2D}), calculated considering the fully developed pressure gradient at the channel outlet

$$\Delta p_{2D} = (F_u + F_d) \cdot \left. \frac{\partial p}{\partial x} \right|_{outlet} \quad (9)$$

$$p_0 = \frac{\Delta p - \Delta p_{2D}}{\Delta p_{2D}} \quad (10)$$

3. NUMERICAL METHODOLOGY

The MHD model implemented in ANSYS CFX solves the equations (1-5) outlined in Section 2 [22]. The problem geometry is modelled using a 3D computational domain. The fluid domain is modelled with the eutectic lithium-lead alloy (LiPb) featuring constant thermophysical properties evaluated at the reference temperature $T_{ref} = 558$ K according to the correlations developed by Jauch et al. [20]. The resulting fluid is characterized by $Pr = 0.034$. The same treatment is applied to the solid domain, modelled with Eurofer according to the correlations outlined by Mergia & Boukos [21] (see Table 2). The Eurofer electrical conductivity was modified to simulate the perfectly insulating cylinder, as detailed in Table 1.

A constant mean velocity u_0 was employed as initial condition for a 2.5D simulation that produced the fully developed flow condition imposed as the channel inlet BC, whereas at the outlet a zero-pressure setting was specified. The range considered is $Re = [20, 80]$ with the flow being laminar. No-slip BCs are enforced at any solid wall. The range for $Pe =$

[0.68, 2.72] is derived from the inlet mean velocity u_0 . For each Re considered, hydrodynamic simulations were performed to provide reference cases for the study.

In a fusion power plant, the liquid metal will be exposed to high intensity magnetic fields, for which the Hartmann number is going to be $Ha = O(10^3)$. Since no computational MHD code available can perform 3D calculations for this value [25], the magnetic field intensity considered for this work was scaled down to the range $M = [10^1 \div 10^2]$. The applied magnetic field $\mathbf{B} = (0, B_y, B_z)$ is uniform and constant in the channel region. The toroidal component is assumed to be dominant with the field inclination on the toroidal axis being defined as $\alpha = \tan^{-1}(B_y/B_z) = 16^\circ$ [19].

Table 3. Comparison of hydrodynamic drag coefficient and average Nusselt number for $\beta = 0.2$ and $G/d = 0.6375$ [23-24]

Re	C_D		Nu	
	Current work	Ref. [23]	Current work	Ref. [24]
20	3.075	3.000	2.902	2.853
40	2.187	2.100	3.812	3.787
60	1.831	1.800	4.537	4.526
108	1.530	1.500	5.917	5.899

Table 4. Mesh sensitivity results for $Ha = 10$ and $Re = 20$

	G_1	G_2	G_3	G_4	G_5
ϕ	100	120	160	200	240
F_u	24	29	39	49	59
F_d	48	58	77	97	115
$N_{ei} \times 10^6$	0.46	0.68	1.42	2.49	3.96
T_{out}	0.682	0.669	0.675	0.679	0.678
Nu	2.585	2.551	2.567	2.572	2.571
Δp	76.63	76.61	76.58	76.57	76.58

On the solid domain external surface and on the obstacle/liquid metal interface, the normal current density flux is assumed as zero to simulate a surrounding dielectric medium (i.e. air and, inside the pipe, water), which, in turn, gives for the electric potential gradient the condition $\partial\phi/\partial n = 0$. For the liquid metal/solid domain interface, the conservation of potential and current density is imposed ($\phi = \phi_w, \mathbf{J}_n = \mathbf{J}_{n,w}$).

The cylinder wall is kept at a fixed temperature ($T_w = 543$ K), whereas the inlet is at $T_{in} = 573$ K. The solid domain external surfaces and the internal surface of the pipe are adiabatic.

A non-uniform structured mesh is employed with an increased refinement in the area surrounding the cylinder to better capture the phenomena happening in this region and to resolve the boundary layers. Since the layer thickness scales with a law $O(M^{-1})$, when approaching fusion blanket conditions 3D MHD simulations become extremely expensive due to the large computational grids required and slow convergence speeds. However, such boundary layers are characterized by high electric resistance and, whether attached to a conductive wall, play a smaller role in the definition of the flow features due to the shunt of the currents to the less resistive path provided by the solid domain. This phenomenon can be used to obtain acceptable accuracy with significantly coarsened mesh: Subramanian et al. demonstrated that, even

for a fully unresolved Hartmann layer, the error on the pressure gradient calculation is around 1% for $c_w \approx 10^{-2}$ [26]. The mesh employed in this study adopts a fully resolved strategy with 10 nodes for the layer of the, whereas for the duct wall and the conductive obstacle layers the resolution is reduced to 4 nodes. The grid was scaled for each Ha considered to keep a consistent layer resolution throughout the study.

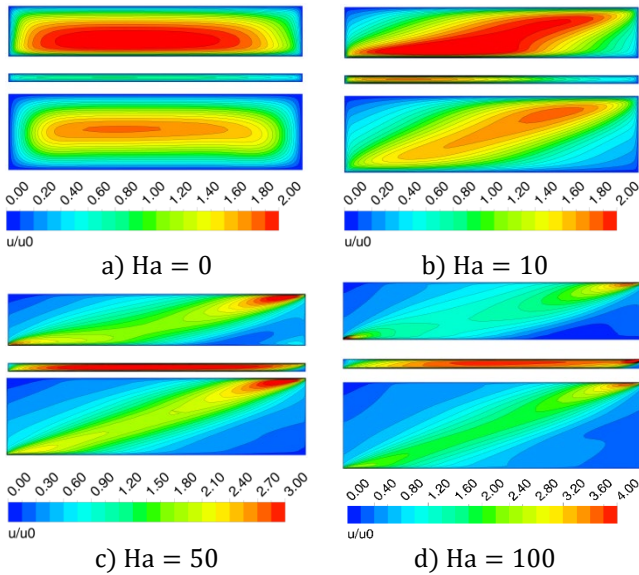


Figure 2. Velocity contour for the flow about the cylinder ($x/d = 0$) and downstream ($x/d = 10$) at $Re = 20$ and increasing **Ha**

The numerical model employed in this study was validated against available data presented in the literature for the flow dynamics and heat transfer of a hydrodynamic flow about an asymmetrically placed circular cylinder [23-24]. The code demonstrated a good agreement for the two parameters considered: the drag coefficient and the average Nusselt number. The results are collected in Table 3. Unfortunately, it was not possible to perform a validation for the MHD model, since the only similar study previously published dealt with high Reynolds numbers [14]. The detailed validation of the pressure-driven MHD flow in a rectangular channel devoid of obstacle is described in Ref. [19].

A mesh sensitivity study was carried over to ensure the independence of the results obtained from the grid resolution for the particular case $Ha = 10$ and $Re = 20$. Five meshes with increasing number of nodes on the cylinder circumference (\emptyset), the upstream (Fu) and downstream (Fd) direction were considered (Table 4). The monitored dimensionless parameters were: the average temperature of the fluid at the outlet (T_{out}), the average Nusselt number on the cylinder surface (Nu) and the pressure drop in the channel (Δp). An error of less than 2% compared with the result of the most refined mesh (G_5) for all the parameters was the selection criterion adopted. Therefore, the mesh G_3 was chosen as the reference for the study.

4. RESULTS AND DISCUSSION

4.1 Channel MHD flow dynamics

For a pressure-driven MHD flow in a rectangular channel, the flow cross section can be separated in three zones: the core

region in the duct centre, where the flow velocity is uniform; the Hartmann boundary layers close to walls perpendicular to the magnetic field of thickness $\delta_H \propto Ha^{-1}$, and the Shercliff boundary layers close to walls parallel to the magnetic field direction of thickness $\delta_S \propto Ha^{-1/2}$. The Shercliff layers are often characterized by high velocity jets with their shape and intensity controlled by the wall conductance ratio.

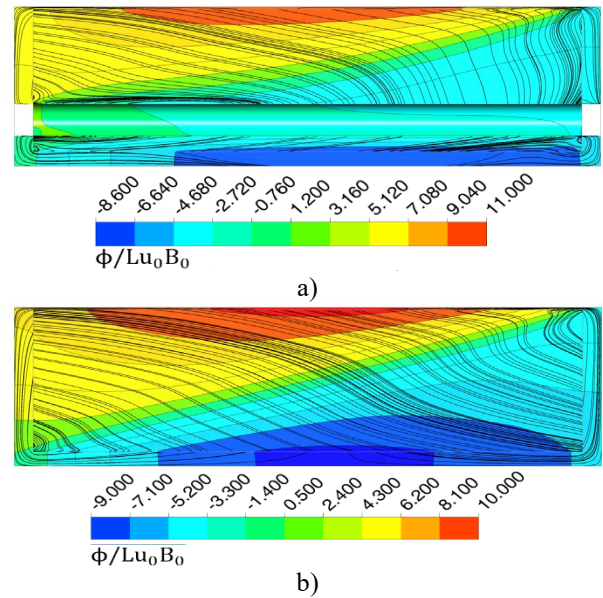


Figure 3. Electric potential contour and current density streamlines for a) the flow about the cylinder ($x/d = 0$) and b) downstream ($x/d = 10$, bottom). Results presented are for **Ha = 100** and **Re = 80**

In the case of skewed magnetic field with $\alpha \gg Ha^{-1/2}$, where α is measured in radians and Ha is expressed using the toroidal half-width of the channel, the Hartmann layer behaviour is observed for each wall with a non-null normal component of the magnetic field [1, 26]. The Shercliff layer flow structures detach from the associated wall and are smeared out into the duct core. From Figure 2a to 2d, this phenomenon can be clearly observed, where the velocity contours for the y - z plane passing through the cylinder centre ($x/d = 0$) and far downstream ($x/d = 10$) are presented. For $\alpha \ll Ha^{-1/2}$, the Shercliff layer behavior is dominant close to the top and bottom wall due to the toroidal magnetic field component being dominant ($B_z \approx 4 \cdot B_y$) and, since these walls are electro-conductive, the formation of jets in the Shercliff layers is observed. Increasing α , the jets detach from the top and bottom wall and coalesce in a single internal one that connects the duct corners parallel to the magnetic field direction and it is separated by the two opposite core regions centred around the other duct corners by free shear layers. For $Ha \rightarrow 100$, the internal jet splits in two distinct velocity peaks close to each corner with the appearance of a saddle point in the duct centre. The non-uniformity of the wall conductance ratio influences the flow features as well with the bottom wall being thicker and more conductive compared with the top one leading to a suppression of the flow in its proximity, which is highlighted by the difference in the velocity peaks in Figure 2d.

The flow distribution on the duct cross-section is directly related to the electric potential one which, in turn, determines the current paths. For the fully developed flow, the electric potential presented in Figure 3b is asymmetrical due to the

contribution of both the toroidal (z) and poloidal (y) component of the magnetic field: the former imposes the dominant top/bottom potential difference and the latter offsets the maximum and minimum away from the duct centreline and toward the duct corners. This effect results in the deformation of the current streamlines which, in turn, generate zones of differential electromagnetic drag on the cross section where the currents are not perpendicular to the magnetic field direction. For instance, current loops are observed close to the duct corners aligned in the magnetic field direction where, since the currents are mostly aligned with the magnetic field, the resistant Lorentz force $F_L \propto J \times B$ is greatly weakened and causes the formation of the jets described earlier (see Figure 2). A similar effect applies on the duct diagonal creating the internal jet and the accompanying free shear layers.

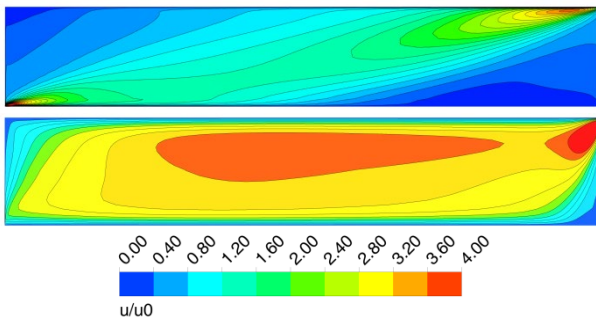


Figure 4. Comparison of the velocity contour for the flow about the cylinder ($\mathbf{x}/\mathbf{d} = \mathbf{0}$) in the upper (top) and lower (bottom) sub-channel for the case $Ha = 100$, $Re = 80$. The lower sub-channel dimension has been magnified by six times in the vertical direction

A comparison between the velocity contour of each sub-channel is presented in Figure 4. The same general behaviour observed for the fully developed flow is found for the flow in the upper sub-channel accounting for the different aspect ratio. Conversely, in the lower sub-channel the current topology is drastically altered to being mostly parallel to the magnetic field direction, and the area is interested by higher velocities compared with the other sub-channel. Moreover, the flow is characterized by a larger core, occupying most of the sub-channel cross-section, and an intense jet in the middle promoted by the insulating obstacle that greatly reduces the electromagnetic drag in the surrounding area.

4.2 Flow pattern about the obstacle

The evolution of the flow pattern about the obstacle in function of Ha and Re is shown in Figure 5 through the velocity streamlines. For the geometrical parameters considered in this study ($\beta = 0.223, G/d = 0.5$), the proximity of the bottom wall perturbrates the cylinder wake and, at the same time, suppresses the vortex shedding and ensures the persistence of the steady regime up to $Re = 80$ [23]. Furthermore, the recirculation bubble that develops is asymmetric with regard to the obstacle midline, being characterized by a larger top vortex and extending farther downstream. When the magnetic field is applied, a reduction of the wake asymmetry and length is observed at first for low intensity ($Ha = 10$), whereas a stronger field completely dampens the vortical structures. Already at $Ha = 50$, a pattern very similar to the hydrodynamic creeping regime is observed for every Re considered. Further increase of the magnetic field

leads to the shifting of the front and rear stagnation points, that move toward the cylinder top. This last phenomenon is particularly evident in Figure 6b where, for $Ha = 100, Re = 80$, a recirculation region is clearly visible around the front stagnation point.

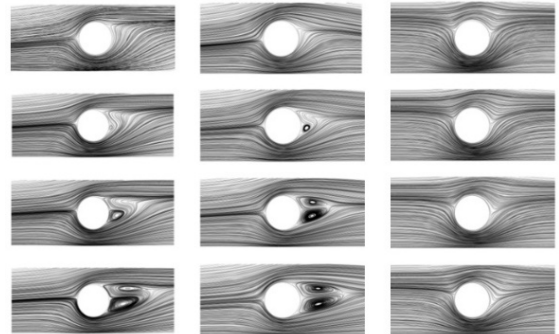
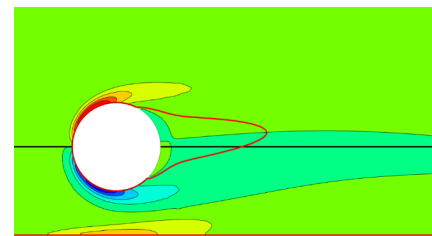
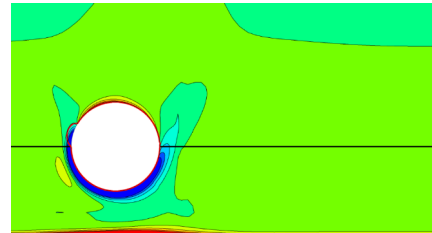


Figure 5. Velocity streamlines around the obstacle for the radial-poloidal plane at $z = 0$. From left to right: $Ha = 0, 10$, and 50 . From top to bottom: $Re = 20, 40, 60$, and 80



a) $Ha = 10, Re = 80$



b) $Ha = 100, Re = 80$

Figure 6. Vorticity contour in the radial-poloidal plane (ω_z , expressed as s^{-1}). Recirculation bubble in the wake is highlighted by a contour line for $u = 0$

The ordinary hydrodynamic behaviour is characterized by a significant imbalance between the mass flow rate carried by the top (Γ_t) and the bottom sub-channel (Γ_b). In Figure 7 it is possible to observe that the latter never exceeds the 10% of the total mass flow rate. This is not surprising, since the bottom sub-channel cross-section amounts to only 16% of the top one. When the magnetic field is applied an additional drag component is introduced that, being independent by the cross-section and much larger than the viscous forces since $Ha \gg 1$, leads to a redistribution of the flow rate. Accounting for the c_w exhibited by the walls of the sub-channels, for $Ha \rightarrow \infty$ the bottom one should carry the 25% of the total mass flow rate. However, it is observed that, already for $Ha = 100$, the bottom mass flow rate exceeds the theoretical value. This discrepancy can be explained by the electroconductive side

walls that, being shared among the sub-channels, allow the leakage of the currents generated in one to close through the other, like it can be observed in Figure 8. This effect causes the coupling of the channels that leads to variations in the flow behaviour such as increased pressure drop and mass flow rate redistribution [27].

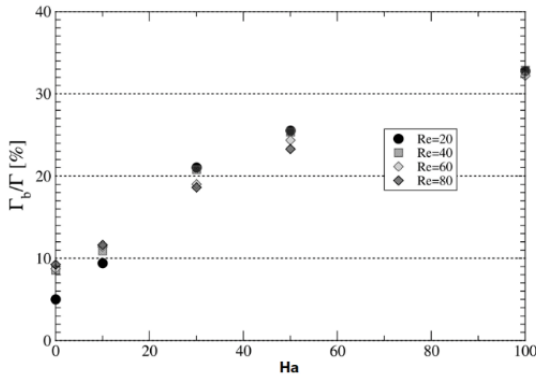


Figure 7. Mass flow rate increase in the bottom subchannel with the Hartmann number (Ha)

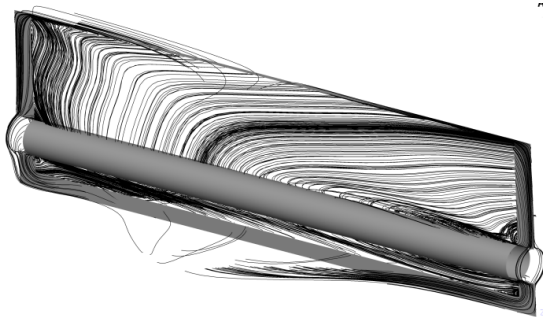


Figure 8. Current streamlines for the toroidal-poloidal plane passing through the obstacle center. Grey overlays mark the solid structures

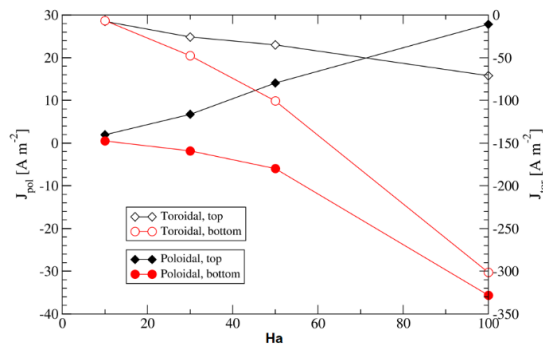


Figure 9. Poloidal (y) and toroidal (z) J in the top and bottom sub-channel versus the Hartmann number (Ha). Data for **Re = 80**

In the case studied, the main coupling effect is the increase of the mass flow rate carried due to the inversion of the y-currents in the bottom channel, which generate a positive - non-resistive to the flow - Lorentz force in the axial direction. At $Ha = 10$, the current density in the channel is low and the coupling is very weak: in both the sub-channels the poloidal current density component is positive ($J_y > 0$), the toroidal one is negative ($J_z < 0$), and, thus, the resulting Lorentz force is resistive, since $F_{L,x} = -(J_y B_z - J_z B_y) \hat{x}$. The two

components agree and sum to each other to give a net resistive force. When the magnetic field increases this is no longer the case, as it can be seen in Figure 9, since the y-component in the bottom sub-channel becomes negative due to the leakage currents contribution, whereas the toroidal component remains negative. The result is a net weakening of the electromagnetic drag experienced by the bottom sub-channel compared with the top one, leading to a mass flow rate surge. However, the flow that develops in the channel will be characterized by higher velocities and, since $J_z \propto u$, it will cause the induction of more intense toroidal currents which, being responsible for the resistive component of the Lorentz force, restore the equilibrium. At $Ha = 100$, the toroidal currents in the bottom sub-channel exceeds by four times the ones calculated above the obstacle. This flow pattern variation leads to a significant effect on the heat transfer that will be described in more detail in Section 4.4.

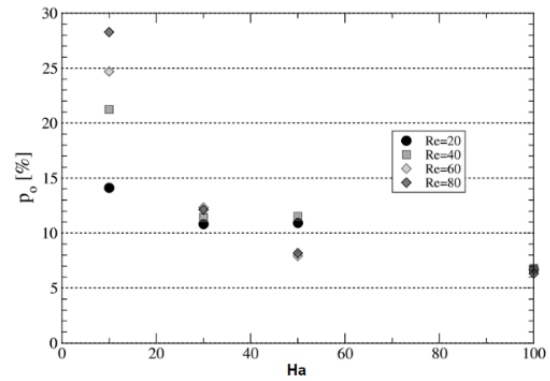


Figure 10. Pressure penalty versus Hartmann number (Ha)

4.3 Pressure drop analysis

For a fully developed flow in a channel devoid of obstacles, the induced currents are confined to the plane perpendicular to the main flow direction and, therefore, are called cross section currents, with the flow being essentially 2D. The obstacle forces the transition from the fully developed state imposed at the inlet to a 3D MHD flow. Significant velocity gradients in the radial (x) and poloidal (y) directions appear which, in turn, translate to electric potential differences that drives currents flowing both upstream and downstream from the obstacle. These interact with the magnetic field causing the generation of a pressure drop term due to the flow three-dimensionality (Δp_{3D}) that adds to the pressure drop for the unobstructed channel (Δp_{2D}).

The term Δp_{2D} is estimated from the pressure gradient for the fully developed flow. For the flow in a rectangular duct, the pressure gradient value is mostly controlled by the conductance ratio of the walls bounding the flow that, for finite conductivity walls, can be expressed by the relation $\partial p / \partial x \approx c_w \sigma u_0 B_0^2$. The term Δp_{3D} strongly depends on the flow geometry and features, therefore no simple relation exists to estimate its intensity. However, since it is related to the magnitude of the radial currents, in general it would be also dependent from the fluid velocity and magnetic field intensity [2].

In Figure 10 the pressure penalty (p_o) is plotted versus the magnetic field intensity. For $Ha \rightarrow 100$, the pressure penalty is found to sharply decrease from around 25% at $Ha = 10$ to 6.5% for the $Ha = 100$ simulations. This trend can be

explained with the Δp_{3D} weaker dependence on the magnetic field intensity compared with Δp_{2D} . This leads to the reduction of the importance of the 3D pressure drop with the increase of the magnetic field, a result consistent with that reported by Hua for a similar configuration [28]. For $Ha = 10$, the pressure penalty is found to vary considerably with the Reynolds number, whereas this effect is no longer observed for $Ha = 100$. The reason for this behaviour can be found in the relative intensity of the inertial forces for a weak magnetic field. The ratio between the electromagnetic and inertial forces is expressed with the interaction parameter $N = Ha^2/Re$. For $N \gg 10$, the flow can be considered inertia-less, and the flow features are controlled only by two parameters, M and c_w . In Figure 11 it can be seen how, since the inertia-less condition is not met, the flow features for $Ha = 10$ are far from being invariant with Re and, thus, the local velocities that directly generate the radial currents responsible for the Δp_{3D} term. Conversely, the velocity contour for $Ha = 100$ are nearly identical, and no discernible spread is found for the pressure penalty data, as shown in Figure 10.

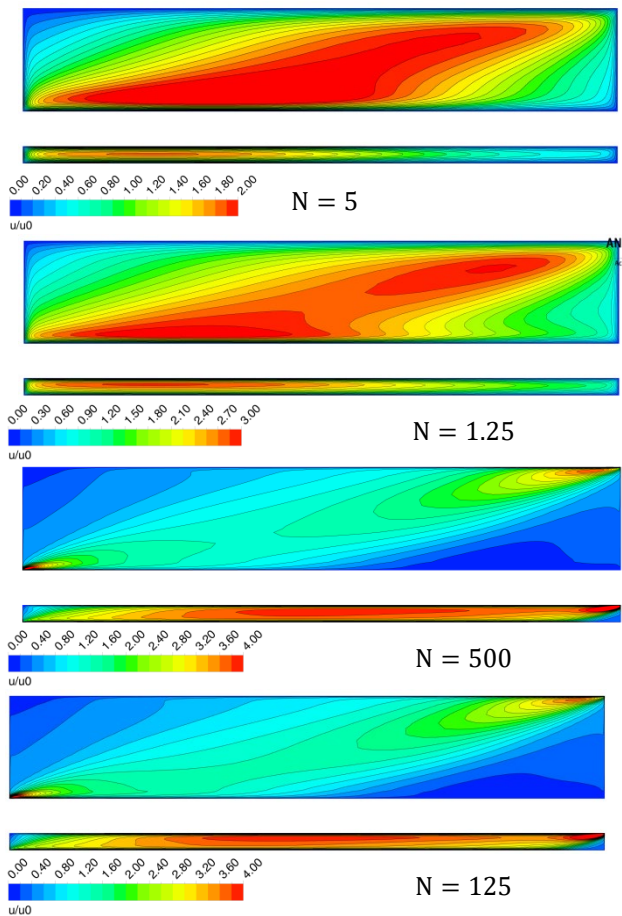


Figure 11. Inertial effects on the velocity contours for the flow about the cylinder. Top: $Ha = 10$, bottom $Ha = 100$. Left: $Re = 20$, right $Re = 80$. View from outlet

4.4 Heat transfer analysis

Since the Joule heating is considered negligible in the inductionless form of the MHD governing equations presented in Section 2, no source of power is present within the channel and the cylinder surface is the only non-adiabatic one: therefore, the magnetic field can alter the heat transfer problem

just through the changes in the channel and obstacle flow dynamics analysed in the previous sections.

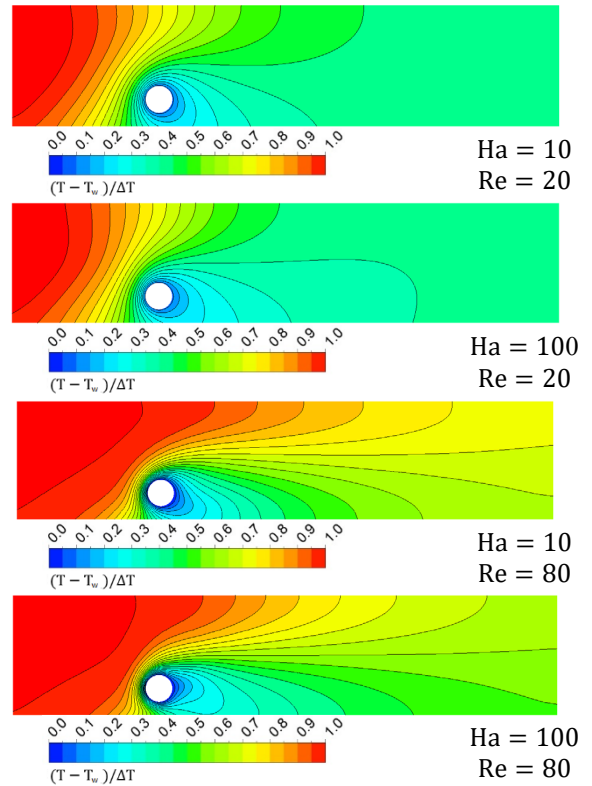


Figure 12. Dimensionless temperature contour comparison for the $z/L = 0$ plane for some selected cases

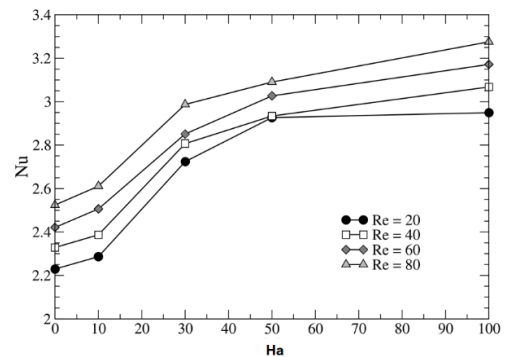


Figure 13. Average Nusselt number vs Hartmann number

For the lowest velocity considered ($Re = 20$), the heat transfer in the channel is dominated by the conduction mechanism ($Pe = 0.68$). In Figure 12 it can be observed how thermal conduction cools the fluid upstream and downstream of the obstacle leading to a complete uniformization of the temperature already for $x/d = 5$. Increasing the magnetic field intensity for this case leads to the warping of the isotherms downstream and toward the duct centreline, due to the enhanced mass flow rate in the bottom sub-channel, which promotes the heat transfer in this region. Conversely, for higher velocities, the convection mechanism becomes more efficient and it can be seen how, for the $Re = 80$ results presented, no relevant cooling of the fluid upstream of the cylinder is observed. The distortion of the isotherms is more pronounced than in the $Re = 20$ case, especially in the cylinder wake, due to the flow transition from the steady vortex to the creeping regime.

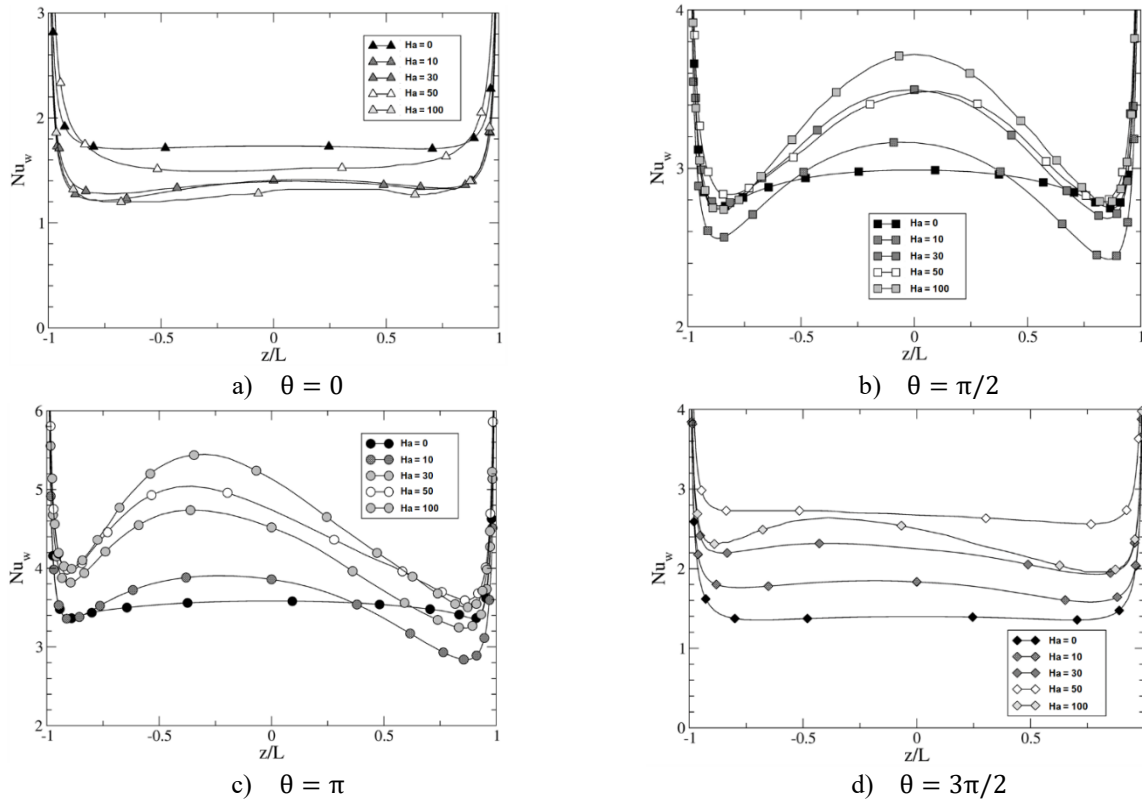


Figure 14. Local Nusselt number as function of the toroidal coordinate for 4 relevant azimuthal positions: a) back, b) top, c) front, d) bottom of the cylinder. Results for $Re = 20$

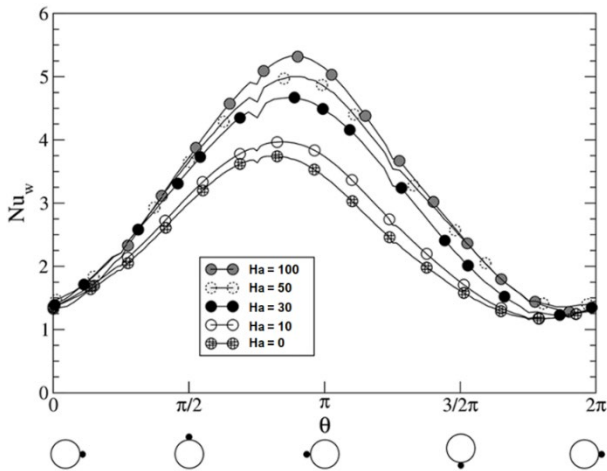


Figure 15. Local Nusselt number on the obstacle circumference at $z/L = 0$ for $Re = 20$ as function of the azimuthal coordinate θ . The back of the obstacle is identified by the coordinate $\theta = 0$

The average Nusselt number computed with Eq. (8) is found to increase with the intensity of the applied magnetic field throughout the Re range considered, as it can be observed in Figure 13, and, for constant Ha , to be also dependent on the Re . The enhancement of the heat transfer with increasing Re is not surprising due to the better efficiency of the convection mechanism with the higher flow velocity. The influence of the magnetic field is more complex to understand due to the many variations introduced in the flow pattern and the significant differences in the flow features for increasing Ha . In Figure 15, the local Nusselt number plotted on the cylinder circumference on the x - y plane $z/L = 0$ shows that the maximum heat transfer is

observed for the frontal part of the obstacle, whereas it steadily decreases moving toward the back due to the reduced ΔT among the fluid and the heating element. This general behaviour is shared by both the OHD and MHD regime.

Conversely, in the back of the cylinder (see Figure 14a) the magnetic field dampening effect on the cylinder wake reduces the heat transfer compared with the hydrodynamic case, whereas in other areas the heat transfer is generally increased. The promoted flow in the bottom sub-channel nearly doubles the Nusselt number between $Ha = 0$ and $Ha = 100$ (see Figure 14d). The departure from the hydrodynamic regime is evident also at the top ($\theta = \pi/2$) and front ($\theta = \pi$) of the obstacle (see Figure 14b and Figure 14c). The local Nusselt number is almost constant for $Ha = 0$ over the toroidal length of the cylinder, whereas the modifications introduced in the flow pattern drastically alter this trend for $Ha > 0$. At the top, a peak is observed at the obstacle centre accompanied by a reduced heat transfer close to the lateral walls. A similar trend is found at the cylinder front, where the quicker fluid in the internal layer close to the wall at $z/L = -1$ enhances the heat transfer compared with the slow flow observed in the opposite wall.

The heat transfer increase is mostly related to the surge in the mass flow rate carried by the bottom sub-channel, which can be explained with the leakage currents originated in the top-channel that enter the region through the shared electroconductive lateral walls. These currents generate a Lorentz force that it is not resistive to the flow movement but actively weakens the retarding action exerted by the currents generated in lower the sub-channel, which in turn leads to the development of jets with velocity much higher than the one observed in the upper sub-channel. It is difficult to foresee if this trend will be maintained at values of the Hartmann number higher than the one considered in this study, but it is

safe to assume that increasing the magnetic field intensity will cause a stronger electromagnetic coupling and, therefore, an increase in the flow rate in the bottom sub-channel. However, this will reduce the mean flow velocity in the top sub-channel, leading to the gradual weakening of the leakage currents generated there and, thus, of the flow-promoting Lorentz force responsible for the surge in the mass flow rate below the cylinder. For $Ha \rightarrow \infty$, this phenomenon will probably lead to an equilibrium between the flow rate of the sub-channels and, therefore, to a Nusselt number no longer function of the magnetic field intensity.

5. CONCLUSIONS

The flow features and heat transfer for a 3D MHD flow past a circular cylinder were investigated for $20 \leq Re \leq 80$; $0 \leq Ha \leq 100$, $\alpha = 16^\circ$ and $c_o = 0$. The main results outlined were:

- The mass flow rate carried by the lower sub-channel is found to increase with the magnetic field intensity due to leakage currents from the upper sub-channel. This phenomenon generates a flow-promoting Lorentz force which tends to equalize the mass flow rates above and below the obstacle.
- For increasing Ha , the pressure penalty due to the obstacle is strongly reduced and becomes independent from the Re . For $Ha = 100$, it amounts to about 6% of the total pressure drop in the channel, approximately an equivalent length $l_{2D} = 1.23 d$ in terms of 2D pressure drop. The contribution to the pressure drop from the 2D flow is expected to become even more dominant at $Ha = 10^3$.
- Due to the enhanced mass flow rate in the lower sub-channel, the average Nusselt number is found to increase with the Hartmann number ($\approx 25\%$ for $Ha = 100$). It is suggested that for $Ha > 100$ the Nusselt number will eventually become independent of the magnetic field intensity, since a reduction in the increase rate of the Nusselt number between $Ha = 50$ and $Ha = 100$ is already observed in Figure 13.

For the moderate magnetic field intensity investigated in this paper, asymmetrically placed pipes show the potential to perform better than in hydrodynamic conditions due to the enhanced mass flow rate in the bottom sub-channel and limited pressure penalty. However, the analysis should be extended to $Ha = 10^3$ before drawing definitive conclusions on the performances of cooling systems in LM blankets relying on this configuration.

In addition, the effect of buoyancy forces on the temperature field should be investigated, since the intensity of the gradients expected in the blanket due to the neutronic heating could cause the onset of a mixed convection regime and heat transfer enhancement. Similar studies have already been conducted for configurations involving horizontal U-pipes and vertically aligned flows [29], but no results are available in the literature for a temperature gradient placed in the stream-wise direction and a moderate ($Ha \approx 100$) magnetic field.

ACKNOWLEDGMENT

The authors wish to acknowledge the help and useful

insights provided by Dr. Matteo Nobili in the realization of this work. This study has been carried out within the framework of the EURO fusion Consortium and has received funding from the Euratom research and training programme 2014-2018 under grant agreement No 633053. The views and opinions expressed herein do not necessarily reflect those of the European Commission.

REFERENCES

- [1] Müller U, Bühler L. (2001). Magnetofluidynamics in channels and containers. Springer Business & Media. <https://doi.org/10.1007/978-3-662-04405-6>
- [2] Smolentsev S, Moreau R, Bühler L, Mistrangelo C. (2010). MHD thermofluid issues of liquid-metal blankets: Phenomena and advances. *Fusion Eng. Des.* 85: 1196-1205. <https://doi.org/10.1016/j.fusengdes.2010.02.038>.
- [3] Moreau R, Bréchet Y, Maniguet L. (2011). Eurofer corrosion by the flow of the eutectic alloy Pb-Li in the presence of a strong magnetic field. *Fusion Eng. Des.* 86: 106-120. <https://doi.org/10.1016/j.fusengdes.2010.08.050>
- [4] Kirillov IR, Reed CB, Barleon L, Miyazaki K. (1995). Present understanding of MHD and heat transfer phenomena for liquid metal blankets. *Fus. Eng. Des.* 27: 553-569. [https://doi.org/10.1016/0920-3796\(95\)90171-X](https://doi.org/10.1016/0920-3796(95)90171-X)
- [5] Messaoud H, Bachir M, Djamel S. (2017). Numerical study of mixed convection and flow pattern in various across- shape concave enclosures. *Int. J. Heat Technol.* 35: 567-575. <https://doi.org/10.18280/ijht.350313>
- [6] Ferdows M, Khaleque TS, Bangalee MZI. (2016). Similarity solution on MHD boundary layer over stretching surface considering heat flux. *Int. J. Heat Technol.* 34: 521-526. <https://doi.org/10.18280/ijht.340325>
- [7] Emam TG, Elmaboud YA. (2017). Three-dimensional magneto-hydrodynamic flow over an exponentially stretching surface. *Int. J. Heat Technol.* 35: 987-996. <https://doi.org/10.18280/ijht.350435>
- [8] Abdou M. (2015). Blanket/first wall challenges and required R&D on the pathway to DEMO. *Fusion Eng. Des.* 100: 2-43. <https://doi.org/10.1016/j.fusengdes.2015.07.021>
- [9] Martelli E, Del Nevo A, Arena P, Bongiovì G, Caruso G, Di Maio PA, Eboli M, Mariano G, Marinari R, Moro F, Mozzillo R, Giannetti F, Di Gironimo G, Tarallo A, Tassone A, Villari R. (2017). Advancements in DEMO WCLL breeding blanket design and integration. *Int. J. Energ. Res.* 42(1): 27-52. <https://doi.org/10.1002/er.3750>
- [10] Martelli E, Caruso G, Giannetti F, Del Nevo A. (2018). Thermo-hydraulic analysis of EU DEMO WCLL breeding blanket. *Fusion Eng. Des.* 130: 48-55. <https://doi.org/10.1016/j.fusengdes.2018.03.030>
- [11] Frank M, Barleon L, Müller U. (2001). Visual analysis of two-dimensional magnetohydrodynamics. *Phys. Fluids.* 13: 2287-2295. <https://doi.org/10.1063/1.1383785>
- [12] Dousset V, Pothérat A. (2008). Numerical simulations of a cylinder wake under a strong axial magnetic field. *Phys. Fluids.* 20: 017104.

- <https://doi.org/10.1063/1.2831153>
- [13] Hussam WK, Thompson MC, Sheard GJ. (2011). 00Dynamics and heat transfer in a quasi-two-dimensional MHD flow past a circular cylinder in a duct at high Hartmann number. *Int. J. Heat Mass Transf.* 54: 1091-1100. <https://doi.org/10.1016/j.ijheatmasstransfer.2010.11.013>
- [14] Hussam WK, Sheard GJ. (2013). Heat transfer in a high Hartmann number MHD duct flow with a circular cylinder placed near the heated side-wall. *Int. J. Heat Mass Transf.* 67: 944-954. <https://doi.org/10.1016/j.ijheatmasstransfer.2013.08.081>
- [15] Tassone A, Nobili M, Caruso G. (2018). Numerical study of the MHD flow around a bounded heating cylinder: Heat transfer and pressure drops. *Int. Commun. Heat Mass Transf.* 91: 165-175. <https://doi.org/10.1016/j.icheatmasstransfer.2017.12.010>
- [16] Tassone A, Nobili M, Caruso G. (2017). Magnetohydrodynamic flow and heat transfer around a heated cylinder of arbitrary conductivity. *J. Phys. Conf. Ser.* 923: 012024. <https://doi.org/10.1088/1742-6596/923/1/012024>
- [17] Mistrangelo C. (2006). Three-Dimensional MHD flow in sudden expansions. *KfK 7201*. <http://d-nb.info/98018066x/34/>
- [18] Kim SH, Kim MH, Lee DW, Choi C. (2012). Code validation and development for MHD analysis of liquid metal flow in Korean TBM. *Fusion Eng. Des.* 87: 951-955. <https://doi.org/10.1016/j.fusengdes.2012.02.048>
- [19] Tassone A, Caruso G, Del Nevo A, Di Piazza I. (2017). CFD simulation of the magnetohydrodynamic flow inside the WCLL breeding blanket module. *Fusion Eng. Des.* 124: 705-709. <https://doi.org/10.1016/j.fusengdes.2017.05.098>
- [20] Jauch U, Karcher V, Schulz B, Haase G. (1986). Thermophysical properties in the system Li-Pb. *KfK 4144*. <http://bibliothek.fzk.de/zb/kfk-berichte/KFK4144.pdf>.
- [21] Mergia K, Boukos N. (2008). Structural, thermal, electrical and magnetic properties of Eurofer 97 steel. *J. Nucl. Mater.* 373: 1-8. <https://doi.org/10.1016/j.jnucmat.2007.03.267>
- [22] Ansys Inc. (2013). ANSYS CFX Solver Theory Guide, ANSYS CFX Release 15.0.
- [23] Zovatto L, Pedrizzetti G. (2001). Flow about a circular cylinder between parallel walls. *J. Fluid Mech.* 440: 1-25. <https://doi.org/10.1017/S0022112001004608>
- [24] Mettu S, Verma N, Chhabra RP. (2006). Momentum and heat transfer from an asymmetrically confined circular cylinder in a plane channel. *Heat Mass Transf. Und Stoffuebertragung* 42: 1037-1048. <https://doi.org/10.1007/s00231-005-0074-6>
- [25] Smolentsev S, Badia S, Bhattacharyay R, Bühler L, Chen L, Huang Q, Jin HG, Krasnov D, Lee DW, Mas de les Valls E, Mistrangelo C, Munipalli R, Ni MJ, Pashkevich D, Patel A, Pulugundla G, Satyamurthy P, Snegirev A, Sviridov V, Swain P, Zhou T, Zikanov O. (2015). An approach to verification and validation of MHD codes for fusion applications. *Fusion Eng. Des.* 100: 65-72. <https://doi.org/10.1016/j.fusengdes.2014.04.049>
- [26] Subramanian S, Swain PK, Deshpande AV, Satyamurthy P. (2015). Effect of Hartmann layer resolution for MHD flow in a straight, conducting duct at high Hartmann numbers. *Sadhana - Acad. Proc. Eng. Sci.* 40: 851-861. <https://doi.org/10.1007/s12046-015-0350-1>
- [27] Madarame H, Taghavi K, Tillack MS. (1985). The influence of leakage currents on MHD pressure drop. *Fusion Technol.* 8. <https://doi.org/10.13182/FST85-A40055>
- [28] Hua TQ, Walker JS. (1995). MHD flow in rectangular ducts with inclined non-uniform transverse magnetic field. *Fusion Eng. Des.* 27: 703-710. [https://doi.org/10.1016/0920-3796\(95\)90186-8](https://doi.org/10.1016/0920-3796(95)90186-8)
- [29] Tassone A, Caruso G, Giannetti F, Del Nevo A. (2018). MHD mixed convection flow in the WCLL: Heat transfer analysis and cooling system optimization. *Proc. 30th SOFT Conf., Giardini Naxos, Italy.*

NOMENCLATURE

Latin symbols

A	Cylinder area [m ²]
B	Magnetic induction (intensity) [T]
c _p	Specific heat capacity [J kg ⁻¹ K ⁻¹]
d	Cylinder outer diameter [m]
d _i	Cylinder inner diameter [m]
F	Stream-wise length [m]
G	Distance between cylinder and lower wall [m]
H	Poloidal half-length [m]
J	Current density [A m ⁻²]
k	Thermal conductivity [W m ⁻¹ K ⁻¹]
L	Toroidal half-length [m]
p	Pressure [Pa]
r, θ, z	Cylindrical coordinates [m, rad, m]
x, y, z	Cartesian coordinates [m]
T	Temperature [K]
u ₀	Inlet mean velocity [m s ⁻¹]

Greek symbols

α	Magnetic field inclination [°]
α _t	Thermal diffusivity [m ² s ⁻¹]
β	Blockage ratio [-]
δ	Thickness [m]
ν	Kinematic viscosity [m ² s ⁻¹]
σ	Electrical conductivity [S m ⁻¹]
φ	Electric potential [V]
ω	Vorticity [s ⁻¹]

Dimensionless groups

c	Wall conductance ratio
Ha	Hartmann number
N	Interaction parameter
Pe	Péclet number
Pr	Prandtl number
Re	Reynolds number

Subscripts

b	Bottom wall, bulk
---	-------------------

d, u	Downstream, upstream	s	Side walls
h	Hartmann layer	t	Top wall
in, out	inlet, outlet	w	Wall